Identification of anhydrous $CaCl_2$ and $KCaCl_3$ in natural inclusions by Raman spectroscopy

GRISHINA Svetlana[1], KODĚRA Peter[2], URIARTE Lucas M.[3], DUBESSY Jean[3], ORESHONKOV Aleksandr[4,5], GORYAINOV Sergey[1], ŠIMKO František[6], YAKOVLEV Igor[1]. ROGINSKII Evgenii M.[7]

1: Sobolev Institute of Geology and Mineralogy Siberian Branch of the Russian Academy of Sciences, Koptuyg Avenue 3, Novosibirsk 630090, Russia

2: Department of Economic Geology, Comenius University, Faculty of Natural Sciences, Ilkovičova 6, 842 15 Bratislava, Slovakia

3: Université de Lorraine, CNRS, CREGU, GeoRessources laboratory (UMR 7359), Vandoeuvre-lès-Nancy, BP-70239, F-54506, France

4: Kirensky Institute of Physics, Federal Research Center KSC SB RAS Akademgorodok 50/38, Krasnoyarsk 660036, Russia

5: Siberian Federal University, Svobodniy 79, Krasnoyarsk 660079, Russia

6: Institute of Inorganic Chemistry, Slovak Academy of Sciences, Dúbravská cesta 9, 845 36 Bratislava, Slovakia

7: Ioffe Institute, St. Petersburg 194021, Russia

Keywords: polymorphs $CaCl_2$, Raman spectra, magma-salt interaction, chlorocalcite, daughter mineral, *ab initio* calculations

Author for checking the proof: Koděra Peter

e-mail peter.kodera@gmail.com

ABSTRACT

Anhydrous chlorides - $CaCl_2$, and $KCaCl_3$ (chlorocalcite) were identified as mineral inclusions in halite from the Siberian Large Igneous Province at the contact of magmatic intrusions and evaporates. Chlorocalcite was also found as daughter mineral in polyphase hypersaline inclusions. While Raman spectra of $KCaCl_3$ (chlorocalcite) in natural inclusions are similar to spectra of synthetic analogue, the Raman spectra of natural $CaCl_2$ do not correspond to the published Raman spectra of synthetic $CaCl_2$. Simulations of Raman spectra using *ab initio* density-functional theory (DFT) allowed us to calculate the spectra of individual polymorphs of $CaCl_2$ and to discriminate anhydrous $CaCl_2$ phases in natural inclusions and synthetic $CaCl_2$. In

the spectrum of the *Pbcn* polymorph of $CaCl_2$ twelve different peaks could be identified at 74, 95, 99, 107, 124, 158, 164, 179, 212, 236, 244, 256 cm^{-1} in contrast to five peaks in the spectrum of the *Pnnm* polymorph of $CaCl_2$ at 115, 157, 160, 211 and 252 cm^{-1}. Naturally occurring $CaCl_2$ in inclusions in halite consist of Pbcn polymorph only, which probably results from a mechanical stress on cooling from magmatic to ambient temperatures. However, the Raman spectra of the synthetic $CaCl_2$ corresponds to the *Pnnm* phase with small contributions of the *Pbcn* phase.

Raman spectra of synthetic $KCaCl_3$ with main peaks at 58, 67, 90, 97, 133, 139, 147, 193 cm^{-1} agrees well with the spectra of chlorocalcite in the natural inclusions. Positions of each atom in the $KCaCl_3$ structure were refined using the density-functional theory. There are no imaginary phonon modes for the optimized structure, indicating that the structure of $KCaCl_3$ is stable. Calculated Raman spectrum is in a good agreement with the Raman spectrum of synthetic and natural $KCaCl_3$ samples.

1. INTRODUCTION

Highly saline paleofluids and molten salts are reported from a wide range of geological environments (e.g. Roedder, 1992). It is widely recognized, that chloride-rich brines play an important role in transport and precipitation of metals as well as gems to form economic mineralizations in diverse geological settings, but especially in magmatic-hydrothermal and metamorphic systems (Reyf & Bazheyev, 1977; Kamenetsky et al., 2002; Newton and Manning, 2010; Lecumberri-Sanchez et al., 2015; Giuliani et al., 2017).

Fluid inclusions provide the best available means to characterize the physical and chemical properties of fluids in fossil hydrothermal systems (Naumov et al., 1990, Andreeva et al., 1998, Bodnar et al., 2014). One of the most important high-salinity hydrothermal systems is the geochemical system NaCl-KCl-$CaCl_2$-H_2O that often includes deep-crustal and upper mantle fluids. Chemical analysis of associated fluid inclusions and their daughter minerals can help to understand the connection between magmatic processes and the composition of magmatic-hydrothermal fluids (Audetat et al., 2008). The high salinity fluids and melts, trapped in multiphase fluid inclusions, often host one or more chloride daughter minerals at ambient temperature due to the precipitation of solid salts on cooling of the inclusions from trapping temperatures. Chloride daughter minerals in inclusions from magmatic-hydrothermal environments are mostly reported as NaCl (halite), KCl (sylvite) and several other chloride crystals.

Correct identification of the chloride daughter minerals in brine inclusions enables to constrain the composition of ore-forming paleofluids and can help to understand the ways of transport and precipitation of metals from hydrothermal fluids. However, only a limited number of analytical tools can be applied for their identification due to the typically small size of the daughter minerals (usually a few microns in diameter) and their exceptionally high hygroscopicity on opening of the host inclusions. The prime analytical technique is here the Raman spectroscopy that provides a quick, non-destructive and easy available identification method for their identification by comparison with published Raman spectra of chlorides (see recent reviews of Frezzotti et al., 2012 and Hurai et al., 2015). Furthermore, reference spectra of several other synthetic chlorides have been reported just recently: $CaCl_2$ (Uriarte et al., 2015), $K_3NaMnCl_6$ (Kurosawa et al., 2016) and $KFeCl_3$ (Koděra et al., 2017). However, there is still a lack of published Raman spectra of some less common minerals hosted in fluid inclusions or the published spectra of synthetic minerals are different from those found in fluid inclusions for some reasons.

The goal of this work is to provide Raman spectrum of synthetic $KCaCl_3$ and to understand the differences of Raman spectra collected from synthetic and natural $CaCl_2$ samples. Raman spectra of all these chloride solids have been calculated using *ab initio* density-functional theory (DFT) and compared with those of synthetic solids and those solids in natural inclusions. Naturally occurring anhydrous chloride minerals, found in halite and apatite from the Siberian Large Igneous Province were used for this purpose. The results of this study can be applied for a clear identification of these minerals in highly saline fluid inclusions by Raman spectroscopy.

2. GEOLOGICAL BACKGROUND

The samples with studied inclusions were taken from endogenic deposits of the Siberian Platform (Fig. 1). The Siberian Platform has been subjected to intensive magmatic activity in the Permian to Early Triassic time. The Siberian Traps represent one of the most voluminous flood basalt provinces on the Earth (Burgess & Bowring, 2015). The basement of the Siberian Traps is heterogeneous and consists of metamorphosed Archean and Early Middle Proterozoic formations (Mazurov & Bondarenko, 1997). The sedimentary cover comprises Riphean and Vendian carbonate terrigenous deposits, Cambrian saliferous carbonates, Middle Palaeozoic terrigenous carbonates, Upper Palaeozoic coal-bearing rocks and Lower Mesozoic volcaniclastic sediments (Kontorovich et al., 1997).

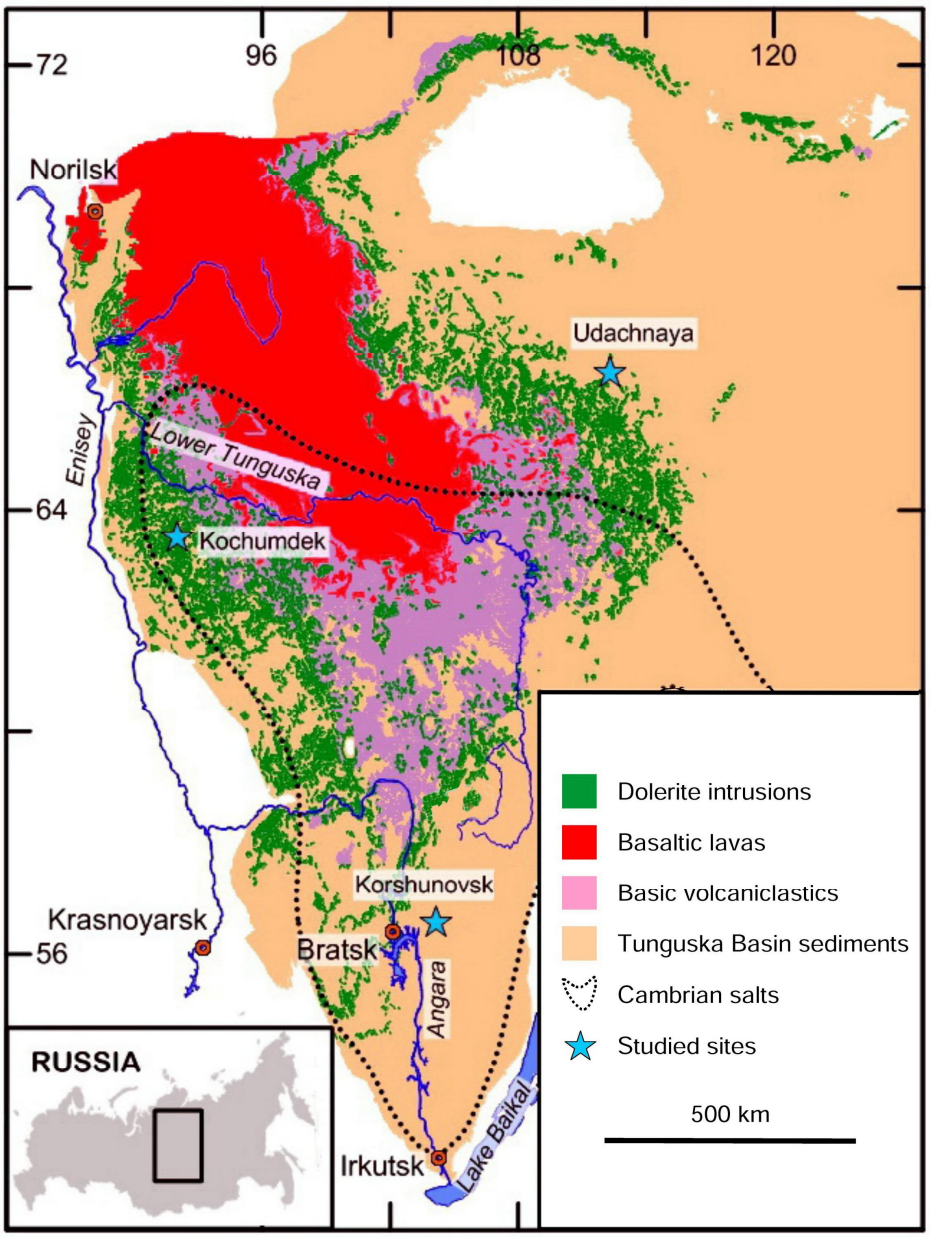

Fig. 1. Sample locations shown on the schematic geological map of the Siberian Large Igneous Province, represented by products of Permian to Early Triassic volcanism, emplaced on the Tunguska basin sediments (Archean to Upper Paleozoic), including the extent of Cambrian saliferous carbonates. Modified from Polozov et al. (2016).

Two main features of geology of the Siberian platform are relevant to this study. One is the widespread occurrence of a thick halite-bearing succession among the Lower Cambrian carbonates. The salt thickness is particularly important in the central and southern platform area where it reaches 350 m. The individual salt beds are 10 to 50 m thick, and are often intercalated with dolomites. The second important feature is the ubiquitous presence of dykes, sills and complex volcanic–tectonic edifices. The lateral extent of individual sills reaches up to several tens to hundreds of kilometers. The thickness of sills is highly variable from a few centimeters up to three hundred meters. The maximum total thickness of intrusive bodies within a

sedimentary sequence, as determined in the northwestern part of the Siberian platform, reaches 1300 m. The emplacement of the high-temperature gas-saturated magma took place over a rather short period during the Permian and Early Triassic. The sills have caused significant alteration of the sedimentary rocks. The volcanic–tectonic edifices cut through the sedimentary cover from the Vendian to the Lower Triassic and are rooted in the crystalline basement (Mazurov and Bondarenko, 1997). The Siberian Trap event is associated with mineral deposits of various types, including apatite-magnetite mineralization.

The huge area of the Cambrian evaporite deposits and intense magmatic activity give a unique opportunity to study salt-magma interaction associated with different styles of magmatic intrusions:

I- metamorphosed salts in the vicinity of trap intrusions (Kochumdek);

II- halite-magnetite rocks from volcanogenic edifices (Korshunovsk Fe-ore deposit);

III- chloride segregations in kimberlites (Udachnaya-East kimberlite pipe).

Samples of salts from both I and II environments are external to the magma body and have clearly an evaporite origin (Grishina et al., 1992; Mazurov et al., 2007). The nature of chloride segregations in kimberlites is intensively debated, while a co-magmatic origin of chlorides is mostly suggested (Kamenetsky et al., 2014; Kitayama et al., 2017; D'Eyrames et al., 2017), the evaporitic source of chlorides (i.e. xenoliths) is also proposed (Grishina et al., 2014a, 2014b; Kopylova et al., 2016).

3. SAMPLES

Most studied inclusions are hosted by metamorphosed halite from different endogenic environments of the Siberian Igneous Province. Metamorphosed salts in the vicinity of trap intrusions were studied from a deep borehole in Kochumdek, located close to the Kochumdek River, the right tributary of the Podkamennaya Tunguska River in East Siberia. The Kochumdek sample was taken from a depth of 2900 m, 7 m above a 300 m thickness dolerite sill (Fig.2).

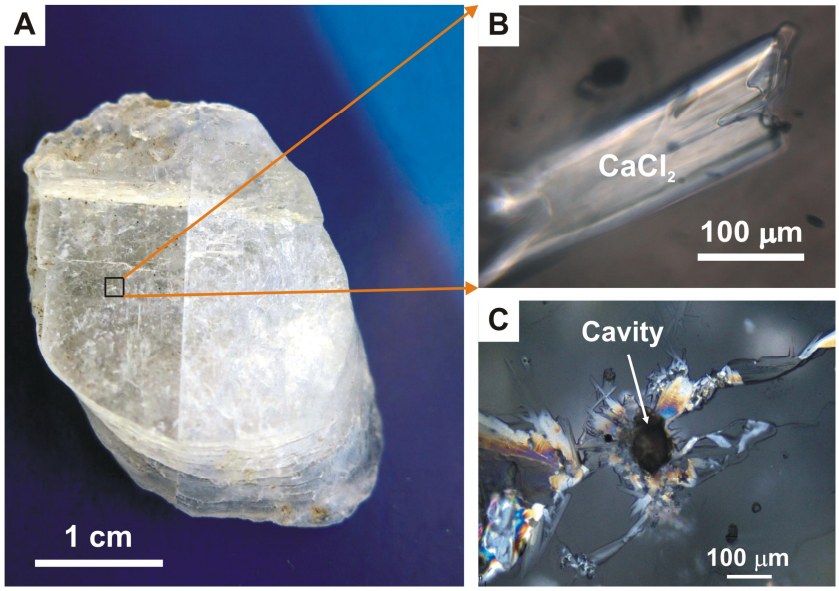

Fig. 2. Images from the rock salt of the Kochumdek borehole: A - core sample from the Kochumdek borehole; B- $CaCl_2$ inclusion in halite (transmitted light); C – cleavage plate surface with empty cavity of exposed $CaCl_2$ inclusion, surrounded by $CaCl_2$-hydrates (reflected light)

Halite-magnetite rock was studied from core samples from the Korshunovsk Fe-ore deposit (Fig. 3A). Cavities filled by halite, a few to 10 centimeters in diameter, are common throughout the magnetite rock and contain euhedral apatite and forsterite crystals (Fig. 3B-E). Unhydrous chlorides were found in halite from cavities, as well as in spatially associated high temperature minerals – in apatite and forsterite.

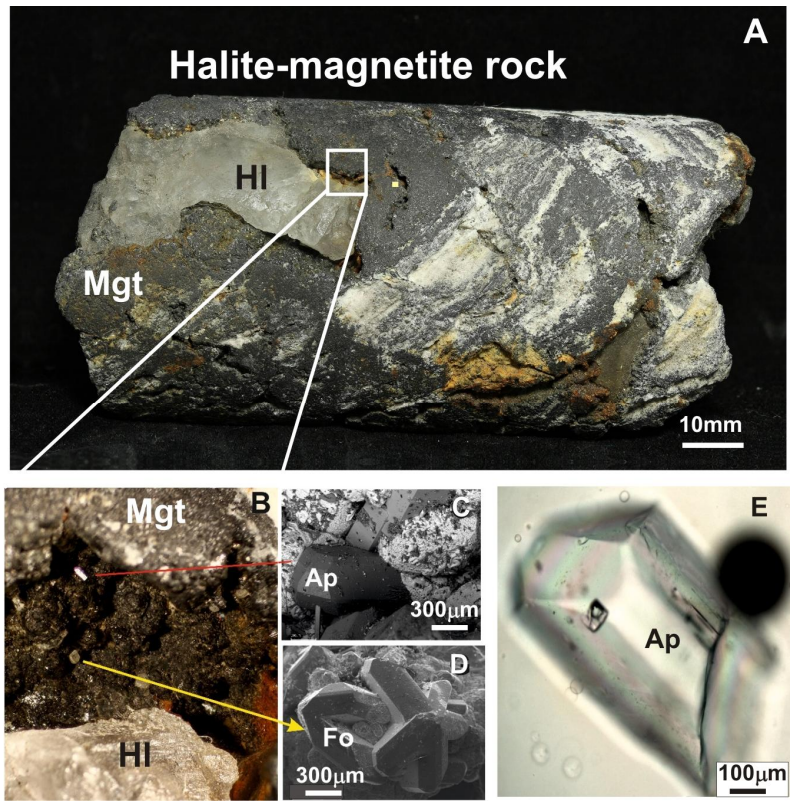

Fig.3. Images from the studied halite-magnetite rock from the Korshunovsk FeO deposit (A) Borehole sample of with halite filling a cavity; (B) Enlarged surface of the cavity, incrusted by euhedral crystals of apatite (C) and forsterite (D) (C and D are SEM images); (E) apatite crystal mounted in epoxy with a polyphase fluid inclusion.

Samples of chloride segregations in unserpentinised kimberlites were collected from stockpiles of the Udachnaya pipe (Fig.4).

Fig. 4. Chloride segregation in kimberlite from the Udachnaya-East pipe.

4. METHODS

From the samples described above, cleavage plates of halite and doubly polished thick sections of apatite crystals (150 to 350 μm thick) were prepared. Fluid inclusion petrography including chronological sequence of fluid inclusions was determined by optical microscopy on an Olympus BX51 microscope combined with an Olympus Color View III camera connected to a PC. The inclusions in apatite and forsterite were exposed to the surface in a water-free environment using oil-based diamond pastes to avoid the loss of water-soluble minerals. After polishing, oil was removed by Petroleum Benzene.

The microthermometric study of CO_2 inclusions was performed on a Linkam stage (model THMS600). The stage was calibrated against the melting points of pure CO_2 inclusions (−56.6°C) and pure water (0°C). Precision of measurements is estimated to ± 0.1°C. The thermometry of inclusions in forsterite and apatite was carried out on a high-temperature heating stage T-1500 (Osorgin & Tomilenko, 1990). This stage was calibrated against the melting points

of synthetic standards : $K_2Cr_2O_7$ (398°C), CsCl (645°C), NaCl (800°C), Au_0 (1063°C), and Mn_0 (1240°C). Precision of measurements is estimated to ± 5°C.

The composition of inclusions was determined by micro-Raman spectrometry and scanning electron micrcoscopy coupled with energy-dispersive X-ray spectroscopy (SEM-EDS) on an Oxford Instruments INCA Energy 350 microanalyzer with a liquid nitrogen-free Large area EDS X-Max-80 Silicon Drift Detector installed on a JEOL JSM-6510LV scanning electron microscope at the Analytical Center for multi-elemental and isotope research SB RAS in Novosibirsk. EDS spectra were collected at an acquisition time of 60 s, an accelerating voltage of 15 kV, a beam current of 1 nA, and a spot diameter of ~1 μm. The EDS spectra were optimised for quantification using the standard XPP procedure included in the INCA Energy 350 software.

The Raman spectra of natural samples were recorded in Novosibirsk on a Horiba Jobin Yvon LabRam HR800 spectrometer coupled to a 1024 pixel LN/CCD detector. Using as excitation source the double harmonic of Nd:YAG solid state laser with a narrow band of nominal wavelength 532 nm and a beam power 30 mW (up to 5 mW on samples; Goryainov et al., 2014). Raman spectra were collected in back-scattering geometry, using an Olympus BX41 microscope. The spectral resolution of the recorded Stokes side of the Raman spectra was set to 2 cm^{-1} at Raman shift of ~300 cm^{-1}. This resolution was achieved by using one grating with 1800 grooves/mm and equal 100 μm slit and confocal pin hole. The microscope was equipped with an Olympus 50x objective lens of WD = 0.37 mm and 0.75 numerical aperture, the focal spot diameter is ~2 μm. The lines from a Ne lamp were used to calibrate the spectrometer. An Edge filter eliminates the Rayleigh scattering which suppressed low-frequency Raman spectrum below 60 cm^{-1} and attenuated the range of 60-100 cm^{-1}. Residual laser beam permiited additional calibration and correction of each recorded spectrum. The spectra were recorded in the -10 to 3800 cm^{-1} range. The accuracy and precision in the wavenumber Raman shift is ±1 cm^{-1}. PeakFit software package was used for deconvolution of Raman spectra into Voigt amplitude contours (Canberra Technical Publications).

For the preparation of synthetic $KCaCl_3$ sample, the following chemicals were used: KCl (Sigma-Aldrich, 99.5%), $CaCl_2$ ($CaCl_2$, Sigma-Aldrich, 99.9%, dried 3 hours at 250^{o}C), all of them of reagent quality. Sample preparation consisted of mixture containing 50 mol% KCl and 50 mol% $CaCl_2$ (molar ratio KCl:$CaCl_2$ = 1:1). Sample was weighted in a glove box under inert atmosphere (Ar, Messer, 99.999% purity), homogenized, then introduced in a platinum crucible and transferred into a preheated furnace at 80^{o}C under dried argon atmosphere. The experiment

was done in tightly closed vertical resistance furnace with water cooling. Thereafter, the sample was heated to 760°C at rate of 5 °C/min. The mixture was kept at this temperature during 1 hour and then cooled to room temperature spontaneously. At the end, the sample was homogenized and analyzed by XRD and Raman methods. The temperature control and the data processing were performed using a computerized measuring device, developed at the Institute of Inorganic Chemistry SAS, Bratislava (Multi-component model for thermal analysis data collections - National Instruments™, where the data collections run on–line under Labview™ software). The temperature of the sample was controlled by a Pt-PtRh10 thermocouple, calibrated on the melting points of pure NaCl and NaF. The accuracy of the temperature difference measurement between the temperatures of primary crystallizations of the given mixtures was ± 1°C.

The X-ray powder patterns of synthetic $KCaCl_3$ were collected at the Institute of Inorganic Chemistry, Slovak Academy of Sciences on a PanAnalytical diffractometer equipped with a curved Ge (111) monochromator placed in the primary beam and a linear PSD. In order to achieve a better resolution, Cu Kα radiation was used. The XRD patterns were taken in the 2θ range of 7-90° at room temperature.

Micro-Raman analysis of synthetic $KCaCl_3$ was performed using a DXR SmartRaman spectrometer associated with a DXR Raman microscope (Thermo Scientific). Raman spectra were obtained by rotating the powder sample, immersed in a sealed glass capillary. Spectra were excited at room temperature using the 532 nm line of a Nd:YAG laser, with power emission conditions of 5 mW on the sample surface. Objective lense of 100× with a pinhole or slit aperture of 50 μm was used. Each spectrum was collected with exposure time 5 s and 60 accumulations, in order to eliminate accidental contamination by cosmic radiation. Peak position was calibrated using a 520 cm^{-1} band of Si-wafer and using a neon glow lamp.

Calculation details for Raman spectra of $CaCl_2$

Structural optimization, energy and Raman calculation were carried out by the CASTEP software packet (Clark et al., 2005) basing *ab initio* density-functional theory (DFT). Initial structures of $CaCl_2$ with the space group *Pnnm* (58) (Liu et al., 2007) and *Pbcn* (60) (Tomaszewski, 1992) were fully optimized using the local density approximation (LDA) provided parameterization of Perdew and Zunger (1981) of the numerical results of Ceperley and Alder, 1980. Calculations were performed using Norm Conserving pseudopotentials with 3s3p3d4s electrons used as valence for Ca atom and 3s3p3d electrons used as valence for Cl atom. The self-consistent field (SCF) procedure was used with a convergence threshold of 2.0 10^{-8} eV/atom. Geometry optimizations were performed with a convergence threshold of 0.005

eV/Å on the max force, 0.1 GPa on the max stress, and 0.002 Å on the maximum displacement. Energy cutoff was set to be 1000 eV, and the Brillouin zone was sampled by 4 × 4 × 6 k-points for $CaCl_2$ with space group *Pnnm* and 4 × 4 × 4 points for the $CaCl_2$ with space group *Pbcn* using the Monkhorst-Pack scheme (Monkhorst and Pack, 1976). The phonon spectra at Γ point and Raman tensors were calculated within density functional perturbation theory and finite displacement method (Porezag and Pederson, 1996 and Refson et al., 2006), based on the crystal system type. Raman spectra were simulated by a Lorentzian distribution with fixed HWHM equal to 4 cm^{-1}.

Calculation details for Raman spectra of $KCaCl_3$

All the structural optimization, energy and Raman calculation were carried out by the CASTEP program [1] using the density-functional theory (DFT). Initial orthorhombic structure of $KCaCl_3$ with the space group *Pmna* (62) (Seifert et al., 1985) was fully optimized using the local density approximation (LDA) and gradient corrected (GGA) exchange-correlation functionals PBE and PBESol. The coordinates of atoms were presented without estimated standard deviations (esd) (Seifert et al., 1985), so the bond length precision could not be obtained and quality of Rietveld refinement is unclear.

5. RESULTS

5.1. Description of inclusions

5.1.1. Inclusions in halite

Halite from reaction zones between intrusive magma and salt rocks is characterized by abundant solid chloride and brine inclusions, spatially associated with dense CO_2 inclusions (Fig.5). CO_2-rich phase occurs as intergrowth with chlorides and in isolated monophase inclusions. KCl and $KCaCl_3$ mineral inclusions are ubiquitous in the environments of the three types of magmatic intrusions: at the vicinity of trap intrusions, in halite cavities of magnetite near basaltic diatreme and in halite segregations in kimberlites. Anhydrous $CaCl_2$ solid inclusions were found only in two localities: at Kochumdek in contact with trap intrusion and in halite cavities of magnetite in Korshunovsk iron ore deposit.

Kochumdek deposit contain rare samples preserved contact metamorphic halite while generally metamorphic halite was removed by dissolution during intensive late hydrothermal activity (Warren, 2016). Abundant $CaCl_2$ solid inclusions were found often in intergrowth with $KCaCl_3$ solids. They are spatially associated with liquid CO_2 inclusions and mineral inclusions like periclase, diopside, amphibole, muscovite, quartz, sulphur, chalcopyrite, pyrite and

pyrrhotite. Homogenisation temperatures of CO_2 inclusions to the liquid phase vary from -9 to -15 ºC in halite from Kochumdek (Fig.1 SM). No liquid water was observed visually or by Raman spectroscopy using long acquisition times (30-60 s) and 10 accumulations in this inclusion assemblage.

All the solid inclusions presented in this work are anhydrous chloride inclusions as shown by the absence of OH-streching band in their Raman spectrum. They have rounded, cubic, euhedral or irregular shapes (Fig.5). The size of the inclusions varies from several to 200 µm, sometimes reaching 500-600 µm. Intergrowths between different individual chloride minerals are common (Fig.5-A, D, E, F).

Brine inclusions, containing $KCaCl_3$ as daughter minerals were found in hydrothermally recrystallised halite in the environments of all types of intrusion (Fig. 5-I) and in apatite from Korshunovsk Fe ore deposit.

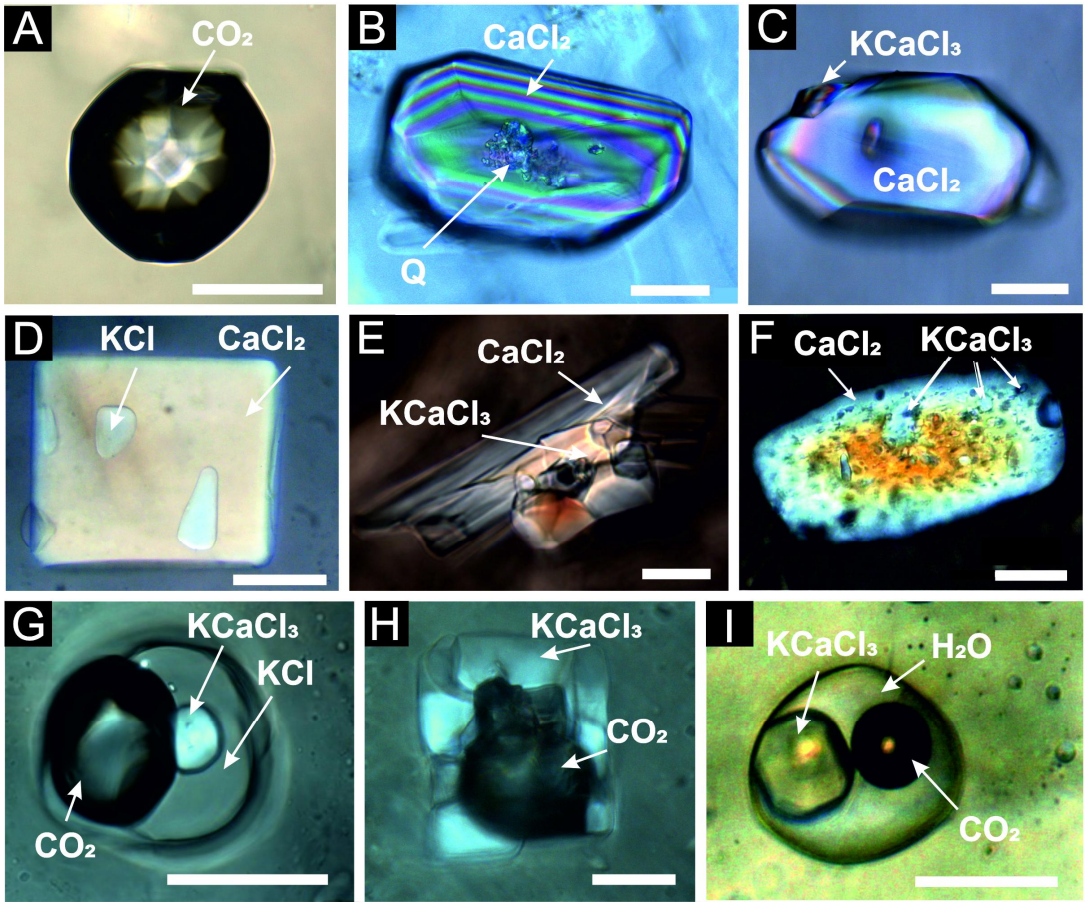

Fig. 5. Photomicrographs of representative anhydrous chloride minerals and coexisting CO_2 inclusions, in halite from different environments: contact with a trap intrusion (A -liquid CO_2 inclusion and B,C-solid $CaCl_2$ inclusion, coexisting in halite from Kochumdek well. Integrowth of different chlorides from the Korshunovsk Fe-ore deposit (D, E, F). Integrowth of chlorides and CO_2 inclusions from chloride xenoliths in Udachnaya-East pipe kimberlites (G, H,) and brine inclusion with KCaCl3 daughter mineral (I). All photomicrographs are in crossed nicoles. Scale bars are 50 µm. Q-quartz

281 5.1.2. Inclusions in apatite and forsterite

282 Apatite and forsterite from the Korshunovsk FeO deposit contain polycrystalline inclusions
283 that have no liquid water at room temperature. According to combined SEM-EDS and Raman
284 analyses their major components are chloride daughter minerals and an unknown Fe-Mg-OH-
285 bearing silicate. Forsterite from Korshunovsk is considered to be a reaction product between the
286 basalt magma and salt-carbonate sedimentary deposits (Mazurov et al., 2007). According to EDS
287 analyses it is quite Mg-rich (Fo_{92-96}).

288 NaCl, KCl and $KCaCl_3$ daughter minerals have been found in apatite hosted inclusions and
289 only NaCl, KCl in forsterite hosted inclusions. Melting of chloride daughter minerals in apatite
290 occured at 400-450 ºC and melting of Fe-Mg-OH-bearing daughter minerals occurs at 500-540
291 ºC. Volume decrease of vapour bubble occured at 600 ºC, and then inclusions decrepitated. Total
292 homogenization was observed in forsterite-hosted inclusions at 720-840ºC.

293 **5.2. Composition of $CaCl_2$-bearing anhydrous inclusions**

294 After opening, solid chloride inclusions transformed immediately to a liquid due to
295 deliquescent properties typical of chloride minerals. Dissolution of $KCaCl_3$ in moisture resulted
296 in formation of KCl crystals and $CaCl_2$ solution. After precipitation generally isotropic crystals
297 form inside the cavity of opened inclusion and mostly anisotropic crystals surround the cavity.
298 The SEM images of products of the incongruent dissolution of $KCaCl_3$ show octahedral crystals
299 in the cavity and a mixture of crystals surrounding the cavity. The elemental composition
300 determined by EDS reveals the presence of K-Cl in octahedral crystals and Ca–K-Cl in the
301 precipitated leachate (Fig. 6). In the case of $CaCl_2$ inclusions only Ca-Cl was identified by EDS
302 analyses in the precipitated leachate around empty cavities (Fig.2C).

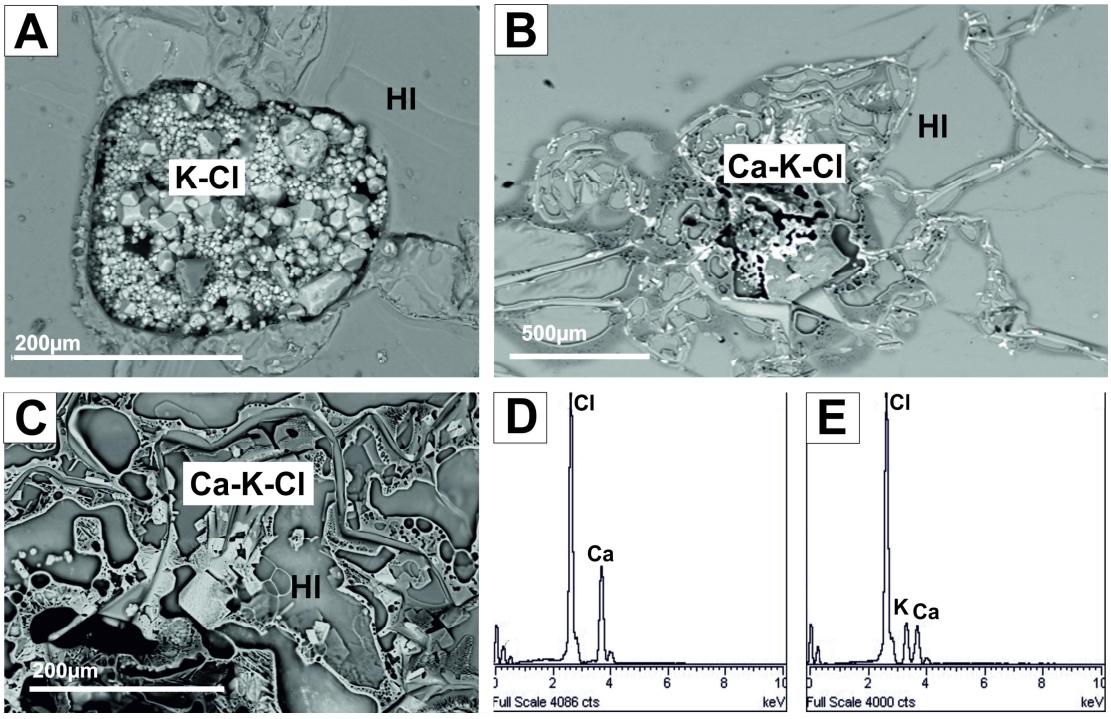

303

Fig.6. Backscattered electron images of $KCaCl_3$ inclusions in halite exposed on air (A, B, C) and representative energy dispersive spectra of the leachate from opened inclusion (D, E), Korshunovsk FeO deposit.

5.3. Raman characterization of natural inclusions

$KCaCl_3$ (chlorocalcite) inclusions are common as daughter minerals in fluid inclusions and as individual mineral inclusions in metamorphosed halite. $KCaCl_3$ was also found in polycrystalline inclusions in apatite from reaction zone of dolerites and salt deposits. The absence of water in these solids was demonstrated by the total absence of symmetric and antisymmetric O-H stretching vibrations in the 2700-4000 cm^{-1} spectral range of the Raman spectra (Fig.2A, SM). Only bands below 300 cm^{-1} have been observed with main peaks at 140, 149 and 195 cm^{-1} wavenumbers which are remarkably constant in between the different samples and match perfectly with the Raman spectra of synthetic $KCaCl_3$ (see below, Fig. 7).

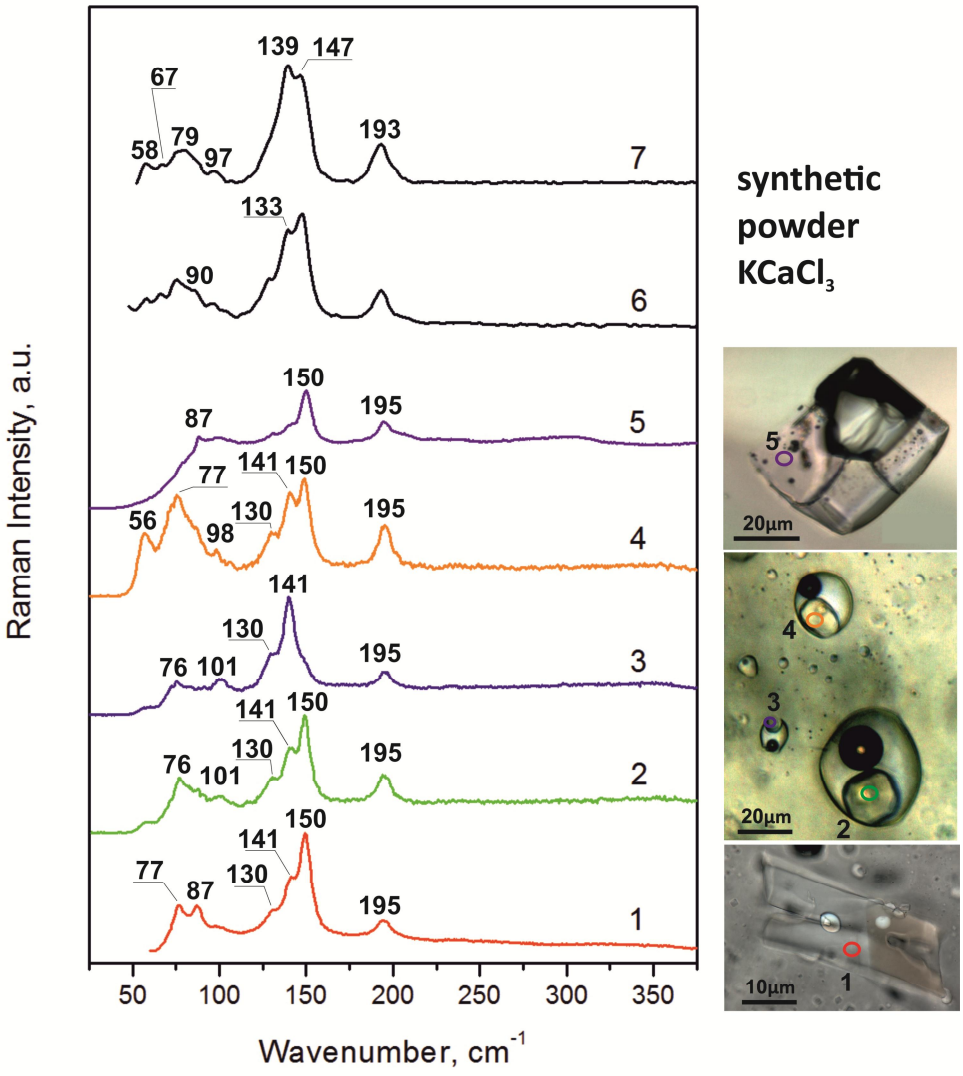

Fig. 7. Comparison of Raman spectra of $KCaCl_3$ from natural inclusions and synthetic powder: 1 - euhedral crystal inclusion in halite (kimberlite pipe Udachnaya-East); 2-4 - daughter minerals inside brine inclusions in halite (kimberlite pipe Udachnaya-East); 5 - daughter mineral in apatite-hosted polyphase inclusion (Korshunovsk Fe-ore deposit); 6, 7 – synthetic $KCaCl_3$ powder.

$CaCl_2$. Almost similar spectra were found in $CaCl_2$ inclusions of samples from two different localities. The Raman spectra of natural inclusions confirms the presence of an anhydrous phase, due to the absence of bands in the water stretching region (2700-4000 cm^{-1}) (Fig.2B, SM). Spectra of inclusions from the two different localities display all same major peaks position in the low frequency region: 74, 95, 99, 107, 124, 158, 164, 179, 212, 236, 244, 256 (Fig. 8). Differences in the relative intensity of the Raman peaks can be seen even in between the spectra of samples from the same location These differences in relative intensity are attributed to different orientations of the crystals in the samples and the anisotropy of the Raman scattering tensor of these crystals. Not all the bands were observed in every spectrum, particularly when Raman signal is too weak to allow minor bands to be detected above the noise level.

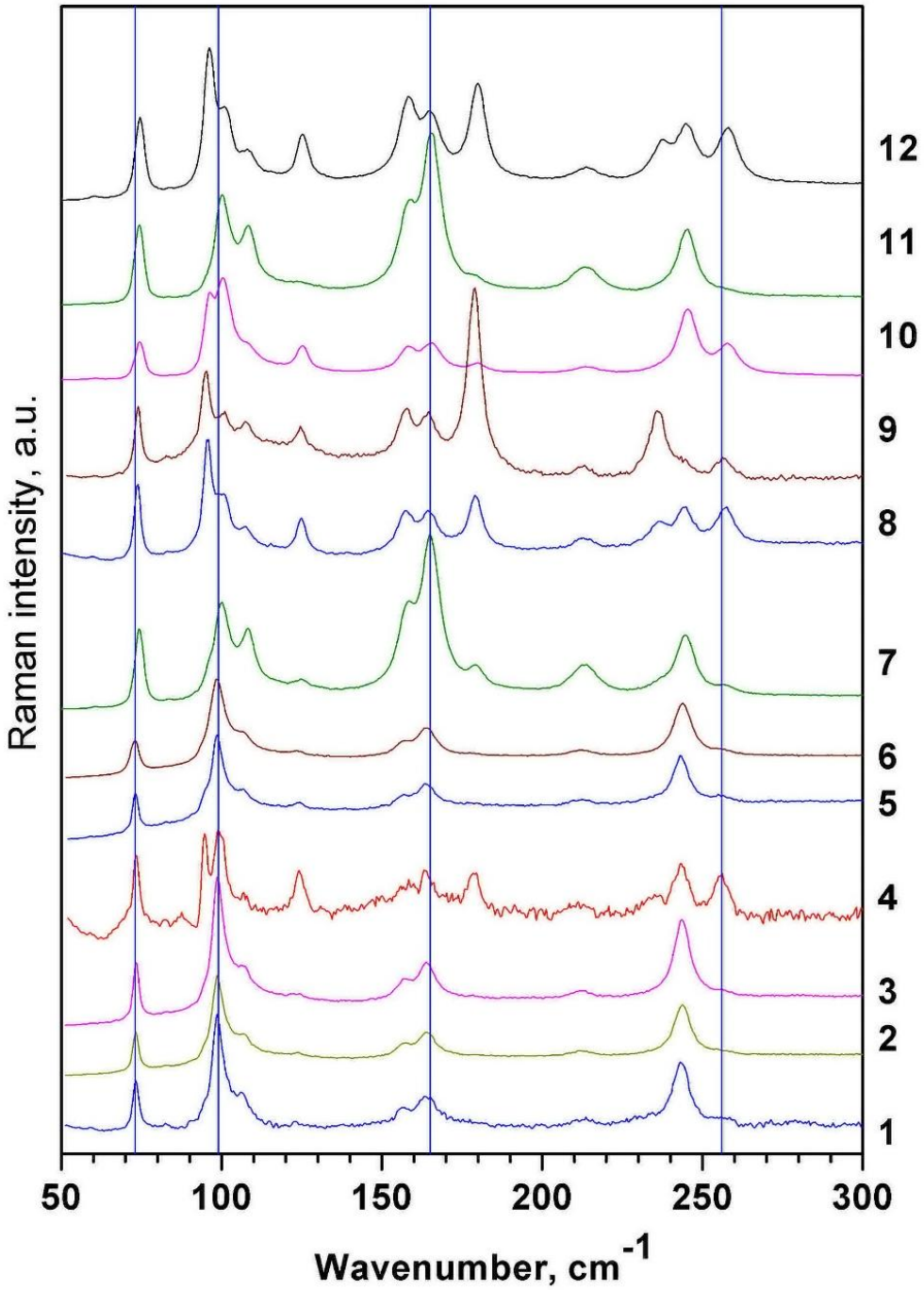

330

331 Fig. 8. Low region Raman spectra of anhydrous $CaCl_2$ inclusions in halite from Korhunovsk FeO deposit (1-9) and
332 Kochumdek borehole (10-12). Vertical lines show Ag modes.

333 As can be seen in Figure 9 the Raman spectra of natural inclusions of $CaCl_2$ are different
334 from reported reference spectra of $CaCl_2$ *Pnnm* polymorph (Uriarte et al., 2015). *Ab initio*
335 calculations were performed to understand the discrepancy of Raman spectra collected from
336 synthetic and natural $CaCl_2$ samples.

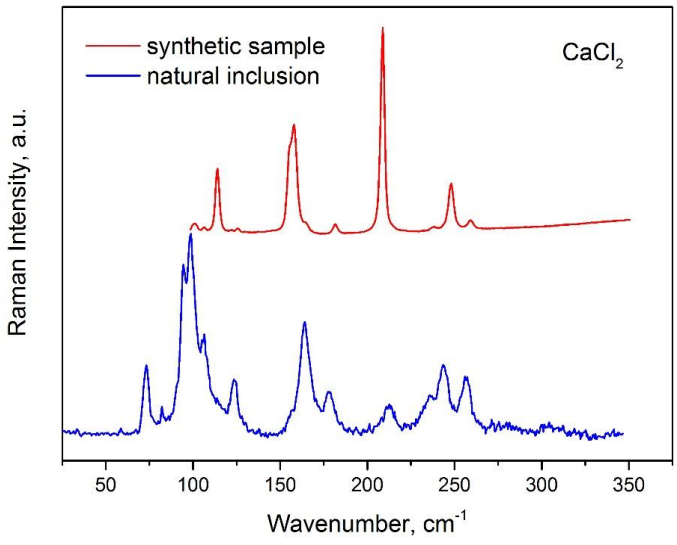

Fig. 9. Comparison of Raman spectra of synthetic $CaCl_2$ (Uriarte et al.,2015) and representative Raman spectra of natural inclusion in halite from the Korshunovsk Fe-oredeposit.

5.4. *Ab initio* computations

The Raman spectra of $CaCl_2$ was calculated for two different polymorphs, with space groups Pnnm and Pbcn. Group theory analysis predicts 6 active Raman modes for the $CaCl_2$ polymorph with *Pnnm* space group: $\Gamma_{raman} = 2A_g + 2B_{1g} + B_{2g} + B_{3g}$. The calculated Raman spectrum for this polymorph consists of 5 peaks and one shoulder (Fig. 10, top). The Pbcn space group polymorph has 18 active Raman modes: $\Gamma_{raman} = 4A_g + 5B_{1g} + 4B_{2g} + 5B_{3g}$ (Table 3), but due to overlapping and low intensity modes the Raman spectrum of this polymorph displays only13 peaks (Fig. 10, bottom).

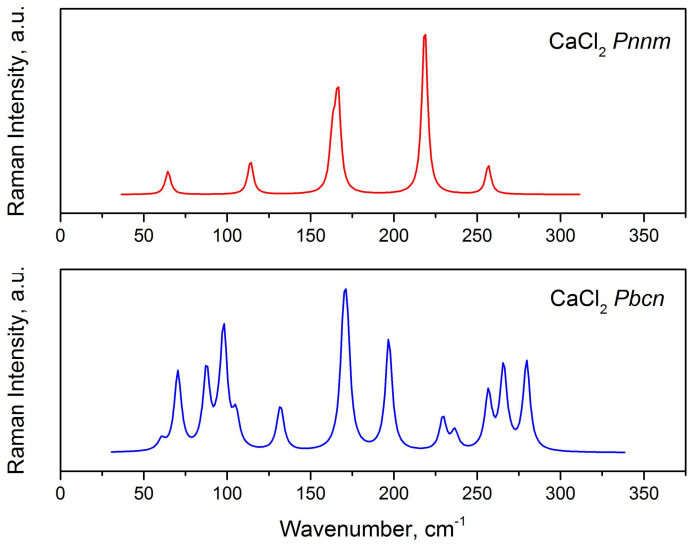

Fig. 10. Calculated Raman spectra of $CaCl_2$ *Pnnm (top)* and *Pbcn (bottom)* phases.

Reported XRD results of synthetic $CaCl_2$ nucleated inside capillaries show the presence of two dehydrated phases, the main phase is hydrophilite, coexisting with the *Pbcn* $CaCl_2$ polymorph

(Uriarte et al., 2015). Crystal structures of both polymorphs of $CaCl_2$ (*Pnnm* and *Pbcn*) are plotted in Fig. 11, using the data of *ab initio* calculations. In both structures, Ca cations are 6-coordinated, whereas Cl anions are 3-coordinated.

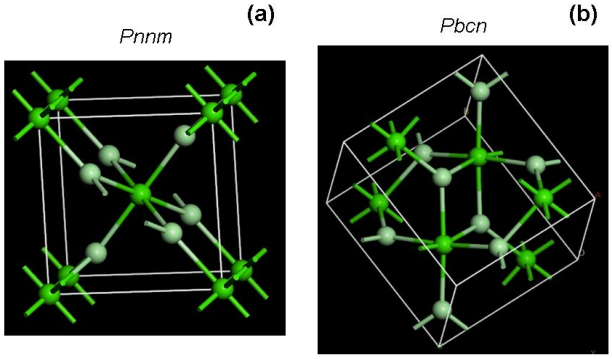

Fig. 11. Structures of two polymorphs of $CaCl_2$: *Pnnm* (a) and *Pbcn* (b). In both structures, Ca cations (dark green balls) are 6-coordinated, whereas Cl anions (light green balls) are 3-coordinated.

As it noted above, there are 6 Raman-active modes for *Pnnm* polymorph and 18 Raman-active modes for *Pbcn* polymorph according to the selection rules for spectra. Thus, two $CaCl_2$ polymorphs can be easily distinguished with Raman scattering spectroscopy due to different numbers of bands. In addition, the intensities and wavenumbers of similar type bands (Ca-Cl stretching, bending etc.) are generally different.

In table 1 the experimental lattice parameters are compared with the ones obtained using DFT for $KCaCl_3$. As can be seen results from theoretical calculations are in a good agreement with experimental data. It is well known, that LDA calculations underestimate equilibrium lattice parameters, while use of the GGA PBE leads to larger lattice parameters (LeSar, 2013) and our calculation results is in agreement with that fact. Thus, calculated bond lengths obtained using LDA are shorter than experimental and longer than experimental in the case of GGA PBESol. In the case of $KCaCl_3$, GGA PBESol approximation predicted lattice constants close to experimental ones. Atomic parameters obtained with PPGA PBESol approximation are presented in table 2.

Table1. Lattice parameters and cell volume of $KCaCl_3$ obtained from experiment and DFT

	experiment	LDA	PBE	PBESol
a, Å	7.561	7.3966	7.6487	7.5362
b, Å	10.48	10.1071	10.5436	10.3498
c, Å	7.255	7.0099	7.3313	7.1748
V, Å	574.9	524.0478	591.2435	559.6301

Table 2. Fractional atomic coordinates of $KCaCl_3$ obtained using GGA PBESol approximation.

	x	*y*	*z*
K	0.42927	0.25000	0.02403
Ca	0.00000	0.00000	0.00000
Cl1	0.19986	0.05513	0.30459
Cl2	0.53366	0.25000	0.60626

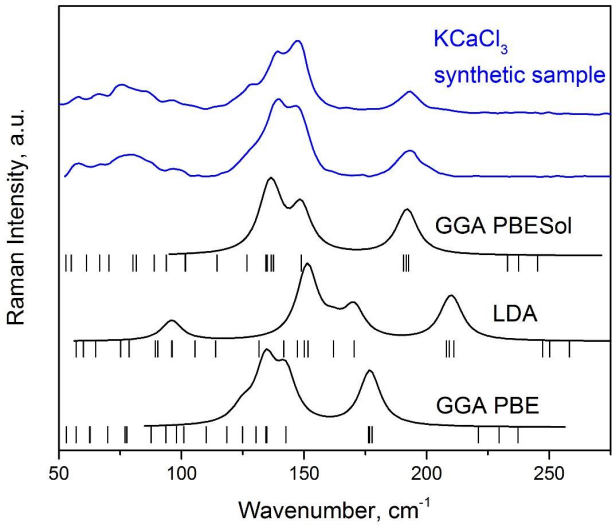

Fig.12. Comparison of observed Raman spectra of $KCaCl_3$ synthetic sample with calculated using GGA PBESol, LDA and GGA PBE approximations.

The Raman spectra calculated by CASTEP code are comparable with the experimental spectra of synthetic sample of $KCaCl_3$ (Fig. 12). There are no imaginary vibrational modes (negative frequencies) for all used approximations, thus, calculated structures of $KCaCl_3$ are stable. It is clear that there is a good agreement between experimental spectra and the calculated one using GGA PBESol approximation, thus, calculated lattice parameters and atomic coordinates could be used for description of crystal structure of synthetic $KCaCl_3$.

Synthesis of $KCaCl_3$ solid:

The complex $KCaCl_3$ is congruent, existing in the simply binary system KCl–$CaCl_2$ at the molar ratio KCl:$CaCl_2$ = 1:1 (Fig. 3 SM). The sample has been analyzed by XRD method. The pattern of this sample is showed in Fig.4 SM), confirming that the sample is a single-phase product.

6. DISCUSSION

Due to similarities in their structure, the majority of anhydrous chlorides displays similar Raman spectra. Thus, positive identification of an unknown daughter mineral in inclusion must be supported by a good fit of all major peaks in terms of their position. This can be obtained by various approaches, including reference to Raman spectrum of a synthetic compound at ambient and/or low temperature and reference to calculated Raman spectrum based on structural data.

6.1. Identification of $CaCl_2$

$CaCl_2$ (*Pnnm*) has phase transition sequence which is unique among the AX_2 compounds, in a narrow pressure range transform from $CaCl_2$ (*Pnnm*) into four different phases α -PbO_2 (*Pbcn*), EuI_2 (*P*2_1/*c*), SrI_2 (*Pbca*), and $PbCl_2$-type (*Pnma*) structures (Leger et al., 1998). Naturally occuring $CaCl_2$ (*Pnnm*) (hydrophilite) was discredited and considered to be either antarcticite ($CaCl_2$·6H2O) or sinjarite ($CaCl_2$·$2H_2O$) (Burke, 2006).

According to the DFT calculations of Raman spectra, we attribute the strong peaks in the published spectrum (Uriarte et al.,2015) of the synthetic $CaCl_2$ to vibrations of the *Pnnm* polymorph and weak lines to vibrations from the *Pbcn* polymorph (Fig.14). As can be seen the calculated vibrational frequencies of $CaCl_2$ polymorphs agree well with experimental results on synthetic $CaCl_2$.

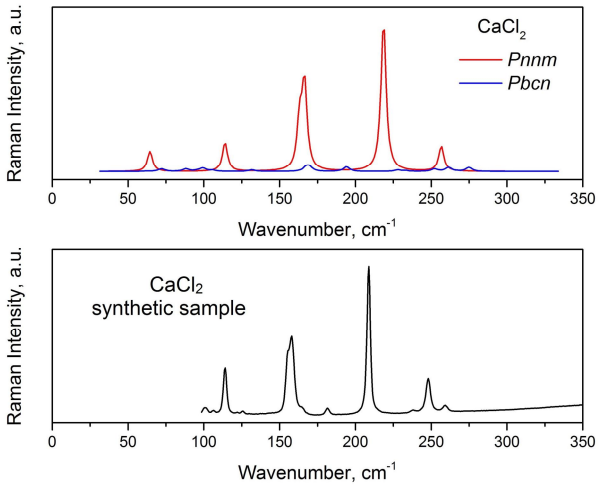

Fig. 14. Calculated Raman spectra of two polymorphs (top) of $CaCl_2$ and measured Raman spectra of synthetic $CaCl_2$ at -172°C (bottom; Uriarte et al., 2015). In order to obtain a better agreement of the simulated Raman spectra of both $CaCl_2$ polymorphs with the spectrum of synthetic mixture of polymorphs, the intensity of the simulated spectrum of the Pnnm polymorph was reduced 10 times.

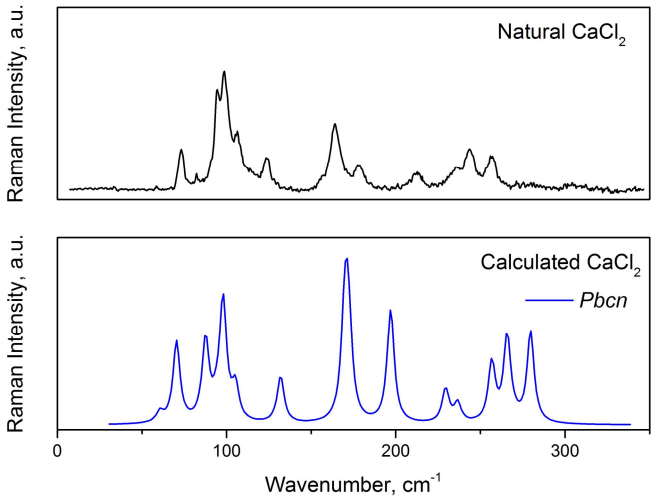

Fig. 15. Comparison of the calculated Raman spectrum of natural $CaCl_2$ hosted by a fluid inclusion in halite (Korshunovsk Fe-ore deposit) with calculated spectrum of the Pnnm polymorph.

In Table 3 and Figure 15 the Raman spectrum of natural $CaCl_2$ hosted by an inclusion in halite from the Korshunovsk Fe-ore deposit is compared to the calculated Raman spectrum of the *Pbcn* polymorph. Apparently, the peaks intensity and wavenumbers are similar to the calculated *Pbcn* polymorph. The vertical lines in Fig. 8 correspond to the symmetric A_g modes at 73, 99, 165 and 256 cm^{-1} of the calculated *Pbcn* phase. The total symmetric A_g modes often exhibit strong Raman intensity, although several B_{1g}, B_{2g} and B_{3g} modes also show a high intensity (Fig. 8). Note that, all Raman spectra from natural $CaCl_2$ inclusions from this study display a similar Raman shift for all major peaks in the spectra of Figure 8. As explained above the different band intensities for different samples and positions within one sample are attributed to non-fixed orientation of crystals with respect to the direction of the electric field of the exciting laser beam and the anisotropy of Raman scattering tensor of the *Pbcn* phase.

Table 3. Comparison of frequencies of Raman active phonon modes of calculated, synthetic (Uriarte et al., 2015) and natural $CaCl_2$ samples.

Synthetic $CaCl_2$, (Uriarte et al., 2015) exp.	Natural $CaCl_2$ (this work), exp.	*Pbcn, DFT*		*Pnnm, DFT*	
v, cm^{-1}	*v*, cm^{-1}	*Irreps*.	ν, cm^{-1}	*Irreps*.	ν, cm^{-1}
		B_{3g}	61	A_g	65
		A_g	70		
		B_{1g}	88		
		B_{3g}	94		
		B_{2g}	97		
		A_g	98		
107 115 125	108 124	B_{1g} B_{1g}	105 131	B_{1g}	114
157	158			B_{3g} B_{2g}	163 166
162	165	A_g	170		
	179	B_{2g}	172		
182	212	B_{3g}	197		
211				A_g	218
		B_{2g}	229		
238	244	B_{1g}	236		
252				B_{1g}	257
260	256	B_{3g} A_g	257 266		
		B_{2g}	270		
		B_{3g}	271		
		B_{1g}	280		

The conditions of $CaCl_2$ formation are different for studied synthetic and natural samples. Natural $CaCl_2$ inclusions in the studied halite samples were most likely formed from a melt. Numerical estimation temperature of halite crystallisation in the vicinity of intrusion is 600-700 ºC (Kontorovich et al., 1997). This temperature interval is higher than the eutectic temperature in the system NaCl-KCl-$CaCl_2$ (Rober et.al., 1975) which indicates that the crystallization of $CaCl_2$ inclusions occurred from an anhydrous ionic salt melt. $CaCl_2$ crystals grown from the melt are sensitive to mechanical stress and may undergo transformation to an α-PbO_2-type structure, which is metastable at room temperature (Anselment, 1985). Such stresses may result from the polydomain structure of the particles and increases on cooling in the ferroelastic phase with increasing spontaneous strain (Unruh et al., 1992). The phase transition of $CaCl_2$ from $CaCl_2$ phase (Pnnm, Z = 2) to α - PbO_2 (Pbcn, Z = 4) polymorphs was investigated by the ab initio norm-conserving pseudopotential density functional method (Liu et al., 2007). The transition between the $CaCl_2$ and α -PbO_2 structures happens at 2.9 Gpa (Liu et al., 2007). In the studied natural halite samples much lower pressure (0.5 Gpa) is estimated using the density of coexisting CO_2 liquid inclusions. This indicates that Pbcn phase could not crystallize in the PT conditions at which crystals of $CaCl_2$ and $KCaCl_3$ were formed from the paleomelt. The stresses in natural inclusions might have increased due to increasing spontaneous strain on cooling from 600°C, leading to ferroelastic phase transition at low ambient and high structural phase transition pressures. The starting material for synthesis was $CaCl_2 \cdot 2H_2O$ heated till 140°C and dehydrated to $CaCl_2$ (Uriarte et al., 2015). Formation mechanism of different polymorphs in the synthetic sample is unknown and detailed explanation remains to be studied.

6.2 Identification of $KCaCl_3$

Chlorocalcite is a rare chloride mineral, that was originally found in sublimates from active volcanic fumaroles (Anthony et al., 1997), but it was also recently determined as a minor evaporite mineral at some potash deposits in China and Laos (Li et al., 2015). In fluid inclusions, chlorocalcite was first reported as daughter crystals in fluid inclusions in halite from the Prairie Formation (Lowenstein and Spencer, 1990). Raman spectrum of solid $KCl \cdot CaCl_2$ inclusion in halite at the vicinity of dolerite intrusions have been reported based on tentative identification according to SEM-EDS and ultra-microchemical analysis (Grishina et al., 1992). In non-evaporate rock environment $KCaCl_3$ was described from SEM-EDS in high temperature fluid inclusions in olivine gems from Zabardad (Clocchiatti, 1981) and chlorocalcite was documented by Koděra et al. (2015) from salt melt inclusions hosted in vein quartz in the Biely Vrch porphyry gold deposit; however, their identification was just tentative based on FIB-EDS analyses. In order to provide a tool for unequivocal identification of this mineral in our fluid

inclusions, we have prepared a synthetic analogue of chlorocalcite ($KCaCl_3$) to determine Raman spectrum of this mineral. Furthermore, the Raman spectrum of $KCaCl_3$ was also calculated by *Ab initio* computations, using the structural data of (Seifert et al., 1985).

As shown in Figure 7 and Table 2 (SM), the main Raman scattering bands of chlorocalcite in natural inclusions correspond to main bands and intensity of peaks of potassium calcium trichloride from the synthetic analogue as well as those calculated from structural data. The minor differences are probably related to admixtures in the natural samples and to different orientation of analyzed crystals.

7. CONCLUSIONS

Raman spectroscopy was used to prove the presence of anhydrous $CaCl_2$ and $KCaCl_3$ daughter minerals in natural inclusions hosted by high temperature halite from different endogenic environments of the Siberian Igneous Province.

The presence of chlorocalcite ($KCaCl_3$) was unambiguously determined by the comparison of the Raman spectra of the daughter mineral and synthetic $KCaCl_3$. This was further supported by *ab initio* density-functional theory (DFT) simulations which were used to calculate the theoretical structure and Raman spectra of $KCaCl_3$. Theoretical structure was in a good agreement with previously published data on $KCaCl_3$ structure and the theoretical Raman spectrum with those of natural and synthetic $KCaCl_3$ samples.

In case of $CaCl_2$, the collected Raman spectra from natural inclusions appear to be completely different from those of synthetic samples published in literature. *Ab initio* calculations enabled to solve this discrepancy. $CaCl_2$ (*Pnnm*) has a phase transition sequence which is unique among the AX_2 compounds. Indeed, in a narrow pressure range can crystalize in five different phases. The published Raman spectrum of synthetic $CaCl_2$ is mainly formed by the Pnnm polymorph, which is the most stable phase at room temperature and atmospheric pressure with small contributions of the Pbcn polymorph. Our calculated spectra of both of these polymorphs are in a good agreement with the spectra published in literature. The comparison of Raman spectra of naturally occurring $CaCl_2$ inclusions in halite with the calculated spectra revealed the presence of the *Pbcn* polymorph only. This polymorph is metastable at room PT conditions and it was probably formed on cooling from magmatic to ambient temperatures.

Anhydrous $CaCl_2$ (*Pbcn)*, found in halite from the Siberian Large Igneous Province was unequivocally identified by Raman spectroscopy. This does not contradict to the discreditation of naturally occurring hydrophilite with another space group (*Pnnm*).

IMPLICATIONS

Well-established Raman spectra of anhydrous chlorides ($KCaCl_3$ and $CaCl_2$ with space groups *Pnnm* and *Pbcn*) can be used for identification of daughter minerals in fluid inclusions from hydrothermal-magmatic and metamorphic environments.

ACKNOWLEDGMENTS

The authors are grateful to Dr. Sharigin V. for providing the sample and photograph of chloride segregation from Udachnaya-East pipe and Dr. Polozov A. for drawing the map.

This work is financially supported by the Russian Foundation for Basic Research (grant no. 15-05-09345) and VEGA grant 1/0560/15.

REFERENCES

Andreeva, I.A., Naumov, V.B., Kovalenko, V.I., Kononkova, N.N., 1998. Fluoride-sulfate and chloride-sulfate salt melts of the carbonatite-bearing complex Musgugai-Khuduk, southern Mongolia. Petrology 6 (3), 284–292.

Anselment B, 1985. Die Dinamik der Phasenumwandlung vom Rutil in denCaCl2-Typ am Beispiel de CaBr2 und zur Polymorphie des CaCl2: Thesis, Universitat Kartsruhe.

Anthony, J.W., Bideaux, R.A., Bladh, K.W., and Nicois, M.C., 1997. Handbook of mineralogy. Mineral Data Publishing, Tucson.

Audetat, A., Pettke, T., Heinrich, C.A., Bodnar, R.J., 2008. Special Paper: The Composition of Magmatic-Hydrothermal Fluids in Barren and Mineralized Intrusions. Economic Geology 103 (5), 877–908. doi:10.2113/gsecongeo.103.5.877.

Bodnar, R.J., Lecumberri-Sanchez, P., Moncada, D., Steele-MacInnis, M., 2014. Fluid Inclusions in Hydrothermal Ore Deposits, in: , Treatise on Geochemistry. Elsevier, pp. 119–142.

Burgess, S.D., Bowring, S.A., 2015. High-precision geochronology confirms voluminous magmatism before, during, and after Earth's most severe extinction. Science advances 1 (7), e1500470. doi:10.1126/sciadv.1500470.

Burke, E.A., 2006. A MASS DISCREDITATION OF GQN MINERALS. The Canadian Mineralogist 44 (6), 1557–1560. doi:10.2113/gscanmin.44.6.1557.

Canberra Technical Publications. S506 Interactive Peak Fit User's Manual.

Ceperley, D.M., Alder, B.J., 1980. Ground State of the Electron Gas by a Stochastic Method. Phys. Rev. Lett. 45 (7), 566–569. doi:10.1103/PhysRevLett.45.566.

Clark, R.P., Reinhardt, F.W., 1975. Phase diagrams for the binary systems CaCl2-KCl and CaCl2-CaCrO4. Thermochimica Acta 12 (3), 309–314. doi:10.1016/0040-6031(75)85044-1.

Clark, S.J., Segall, M.D., Pickard, C.J., Hasnip, P.J., Probert, M.I.J., Refson, K., Payne, M.C., 2005. First principles methods using CASTEP. Zeitschrift für Kristallographie - Crystalline Materials 220 (5/6), 191. doi:10.1524/zkri.220.5.567.65075.

Clocchiatti R, Massare D, Jehanno C, 1981. Origine hydrothermale des olivines gemmes de l'ile de Zabardad (St.Johns) Mer Rouge, par l'etude de leurs inclusions. Bull. Mineral 104, 354–360.

D'Eyrames, E., Thomassot, E., Kitayama, Y., Golovin, A., Korsakov, A., Ionov, D., Danelian, T., Jolivet, M., 2017. A mantle origin for sulfates in the unusual "salty" Udachnaya-East kimberlite from sulfur abundances, speciation and their relationship with groundmass carbonates. Bull. Soc. géol. Fr. 188 (1-2), 6. doi:10.1051/bsgf/2017007.

Frezzotti, M.L., Tecce, F., Casagli, A., 2012. Raman spectroscopy for fluid inclusion analysis. Journal of Geochemical Exploration 112, 1–20. doi:10.1016/j.gexplo.2011.09.009.

Giuliani, G., Dubessy, J., Ohnenstetter, D., Banks, D., Branquet, Y., Feneyrol, J., Fallick, A.E., Martelat, J.-E., 2017. The role of evaporites in the formation of gems during metamorphism of carbonate platforms: A review. Miner Deposita 35 (2), 699. doi:10.1007/s00126-017-0738-4.

Goryainov, S.V., Likhacheva, A.Y., Rashchenko, S.V., Shubin, A.S., Afanas'ev, V.P., Pokhilenko, N.P., 2014. Raman identification of lonsdaleite in Popigai impactites. J. Raman Spectrosc. 45 (4), 305–313. doi:10.1002/jrs.4457.

Grishina, S., Dubessy, J., Kontorovich, A., Pironon, J., 1992. Inclusions in salt beds resulting from thermal metamorphism by dolerite sills (eastern Siberia, Russia). ejm 4 (5), 1187–1202. doi:10.1127/ejm/4/5/1187.

Grishina, S.N., Polozov, A.G., Mazurov, M.P., Goryainov, S.V., 2014a. Genesis of chloride-carbonate segregations of the Udachnaya-East pipe. Dokl. Earth Sc. 458 (1), 1129–1131. doi:10.1134/S1028334X14090141.

Grishina, S.N., Polozov, A.G., Smirnov, S.Z., Mazurov, M.P., Goryainov, S.V., 2014b. Inclusions in chloride xenoliths from the Udachnaya-East Kimberlite. Geochem. Int. 52 (7), 595–603. doi:10.1134/S0016702914050048.

Hurai, V., Huraiová, M., Slobodník, M., Thomas, R., 2015. Geofluids: Developments in microthermometry, spectroscopy, thermodynamics, and stable isotopes / Vratislav Hurai, Monika Huraiová, Marek Slobodník, Rainer Thomas. Elsevier, Amsterdam.

Kamenetsky, V.S., Golovin, A.V., Maas, R., Giuliani, A., Kamenetsky, M.B., Weiss, Y., 2014. Towards a new model for kimberlite petrogenesis: Evidence from unaltered kimberlites and mantle minerals. Earth-Science Reviews 139, 145–167. doi:10.1016/j.earscirev.2014.09.004.

Kamenetsky, V.S., van Achterbergh, E., Ryan, C.G., Naumov, V.B., Mernagh, T.P., Davidson, P., 2002. Extreme chemical heterogeneity of granite-derived hydrothermal fluids: An example from inclusions in a single crystal of miarolitic quartz. Geol 30 (5), 459. doi:10.1130/0091-7613(2002)030<0459:ECHOGD>2.0.CO;2.

Kitayama, Y., Thomassot, E., Galy, A., Golovin, A., Korsakov, A., d'Eyrames, E., Assayag, N., Bouden, N., Ionov, D., 2017. Co-magmatic sulfides and sulfates in the Udachnaya-East pipe (Siberia): A record of the redox state and isotopic composition of sulfur in kimberlites and their mantle sources. Chemical Geology 455, 315–330. doi:10.1016/j.chemgeo.2016.10.037.

Koděra, P., TAKÁCS, Á., RACEK, M., ŠIMKO, F., LUPTÁKOVÁ, J., VÁCZI, T., ANTAL, P., 2017. Javorieite, KFeCl 3: A new mineral hosted by salt melt inclusions in porphyry gold systems. eur.j.mineral. doi:10.1127/ejm/2017/0029-2672.

Kontorovich, A.E., Khomenko, A.V., Burshtein, L.M., Likhanov, I.I., Pavlov, A.L., Staroseltsev, V.S., Ten, A.A., 1997. Intense basic magmatism in the Tunguska petroleum basin, eastern Siberia, Russia. Petroleum Geoscience 3 (4), 359–369. doi:10.1144/petgeo.3.4.359.

Kopylova, M.G., Gaudet, M., Kostrovitsky, S.I., Polozov, A.G., Yakovlev, D.A., 2016. Origin of salts and alkali carbonates in the Udachnaya East kimberlite: Insights from petrography of kimberlite phases and their carbonate and evaporite xenoliths. Journal of Volcanology and Geothermal Research 327, 116–134. doi:10.1016/j.jvolgeores.2016.07.003.

578 Kurosawa, M., Sasa, K., Shin, K.-C., Ishii, S., 2016. Trace-element compositions and Br/Cl ratios of fluid
579 inclusions in the Tsushima granite, Japan: Significance for formation of granite-derived fluids.
580 Geochimica et Cosmochimica Acta 182, 216–239. doi:10.1016/j.gca.2016.03.015.
581 Lecumberri-Sanchez, P., Steele-MacInnis, M., Weis, P., Driesner, T., Bodnar, R.J., 2015. Salt precipitation
582 in magmatic-hydrothermal systems associated with upper crustal plutons. Geology, G37163.1.
583 doi:10.1130/G37163.1.
584 Léger, J.-M., Haines, J., Danneels, C., 1998. PHASE TRANSITION SEQUENCE INDUCED BY HIGH-PRESSURE
585 IN CaCl2. Journal of Physics and Chemistry of Solids 59 (8), 1199–1204. doi:10.1016/S0022-
586 3697(98)00057-2.
587 LeSar, R., 2013. Introduction to computational materials science: Fundamentals to applications /
588 Richard LeSar, Iowa State University. Cambridge University Press, Cambridge, New York.
589 Li, M., Yan, M., Wang, Z., Liu, X., Fang, X., Li, J., 2015. The origins of the Mengye potash deposit in the
590 Lanping–Simao Basin, Yunnan Province, Western China. Ore Geology Reviews 69, 174–186.
591 doi:10.1016/j.oregeorev.2015.02.003.
592 Liu, Y.H., Ma, Y.M., He, Z., Cui, T., Liu, B.B., Zou, G.T., 2007. Phase transition and optical properties of
593 CaCl 2 under high pressure by ab initio pseudopotential plane-wave calculations. J. Phys.: Condens.
594 Matter 19 (42), 425225. doi:10.1088/0953-8984/19/42/425225.
595 Lowenstein, T.K., Spencer, R.J., 1990. Syndepositional origin of potash evaporites; petrographic and fluid
596 inclusion evidence. American Journal of Science 290 (1), 1–42. doi:10.2475/ajs.290.1.1.
597 Mazurov, M.P., Grishina, S.N., Istomin, V.E., Titov, A.T., 2007. Metasomatism and ore formation at
598 contacts of dolerite with saliferous rocks in the sedimentary cover of the southern Siberian platform.
599 Geol. Ore Deposits 49 (4), 271–284. doi:10.1134/S1075701507040022.
600 Mazurov, M.P. and Bondarenko, P. M., 1997. Structural Genetic Model of the Angara–Illim-Type Ore-
601 Forming System,. Geol. Geofiz. 38, 1584–1593.
602 Monkhorst, H.J., Pack, J.D., 1976. Special points for Brillouin-zone integrations. Phys. Rev. B 13 (12),
603 5188–5192. doi:10.1103/PhysRevB.13.5188.
604 Naumov, V.B., Solovova, I.P., Kovalenker, V.A., Rusinov, V.L., Kononkova, N.N., 1990. Crystallization
605 conditions and compositions of silicate and salt melts of the volcanoplutonic complex in the Angren
606 area, Soviet Central Asia.: Trans. (Doklady). USSR Acad. Sci. (5), 199–202.
607 NEWTON, R.C., MANNING, C.E., 2010. Role of saline fluids in deep-crustal and upper-mantle
608 metasomatism: Insights from experimental studies. Geofluids 73, 1597. doi:10.1111/j.1468-
609 8123.2009.00275.x.
610 Osorgin, N., Tomilenko, A., 1990. HEATING STAGE: Patent No. 1562816 of the USSR.
611 Perdew, J.P., Zunger, A., 1981. Self-interaction correction to density-functional approximations for
612 many-electron systems. Phys. Rev. B 23 (10), 5048–5079. doi:10.1103/PhysRevB.23.5048.
613 Polozov, A.G., Svensen, H.H., Planke, S., Grishina, S.N., Fristad, K.E., Jerram, D.A., 2016. The basalt pipes
614 of the Tunguska Basin (Siberia, Russia): High temperature processes and volatile degassing into the
615 end-Permian atmosphere. Palaeogeography, Palaeoclimatology, Palaeoecology 441, 51–64.
616 doi:10.1016/j.palaeo.2015.06.035.
617 Porezag, D., Pederson, M.R., 1996. Infrared intensities and Raman-scattering activities within density-
618 functional theory. Phys. Rev. B 54 (11), 7830–7836. doi:10.1103/PhysRevB.54.7830.
619 Refson, K., Tulip, P.R., Clark, S.J., 2006. Variational density-functional perturbation theory for dielectrics
620 and lattice dynamics. Phys. Rev. B 73 (15), R4954. doi:10.1103/PhysRevB.73.155114.
621 Reyf F.G., B.E., 1977. Magmatic chloride solution and tungsten mineralization. Geochem. Int. (14), 45–
622 51.
623 Roedder, E., 1992. Fluid inclusion evidence for immiscibility in magmatic differentiation. Geochimica et
624 Cosmochimica Acta 56 (1), 5–20. doi:10.1016/0016-7037(92)90113-W.

625 Seifert, H.-J., Fink, H., Thiel, G., Uebach, J., 1985. Thermodynamische und strukturelle Untersuchungen
626 an den Verbindungen der Systeme KCl/MCl2 (M ?: Ca, Cd, Co, Ni). Z. Anorg. Allg. Chem. 520 (1), 151–
627 159. doi:10.1002/zaac.19855200118.
628 Tomaszewski, P.E., 1992. Structural phase transitions in crystals. I. Database. Phase Transitions 38 (3),
629 127–220. doi:10.1080/01411599208222899.
630 Uriarte, L.M., Dubessy, J., Boulet, P., Baonza, V.G., Bihannic, I., Robert, P., 2015. Reference Raman
631 spectra of synthesized CaCl 2 · n H 2 O solids (n = 0, 2, 4, 6). J. Raman Spectrosc. 46 (10), 822–828.
632 doi:10.1002/jrs.4730.
633 Warren, J.K., 2016. Magma-Evaporite-Hydrothermal Metal Associations, in: Warren, J.K. (Ed.),
634 Evaporites. Springer International Publishing, Cham, pp. 1591–1657.

Supplementary material

Identification of anhydrous $CaCl_2$ and $KCaCl_3$ in natural inclusions by Raman spectroscopy

GRISHINA et al.

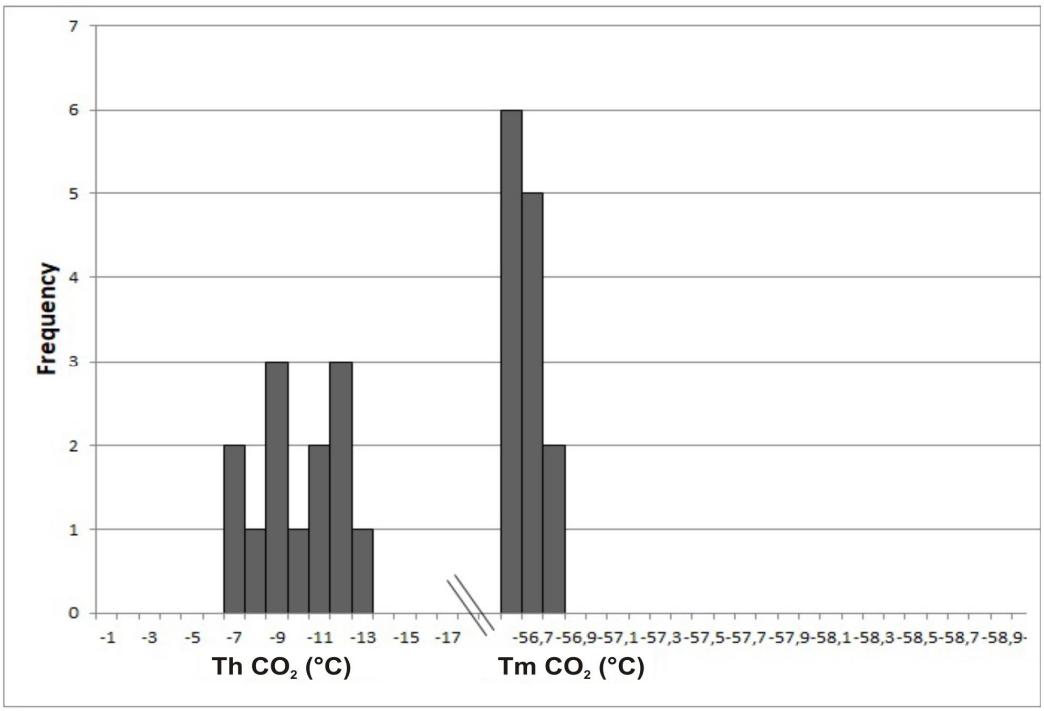

Fig. 1 SM. Histogram of homogenization temperatures (Th) and melting temperatures (Tm) of CO_2 inclusions from the Kochumdek rocksalt sample.

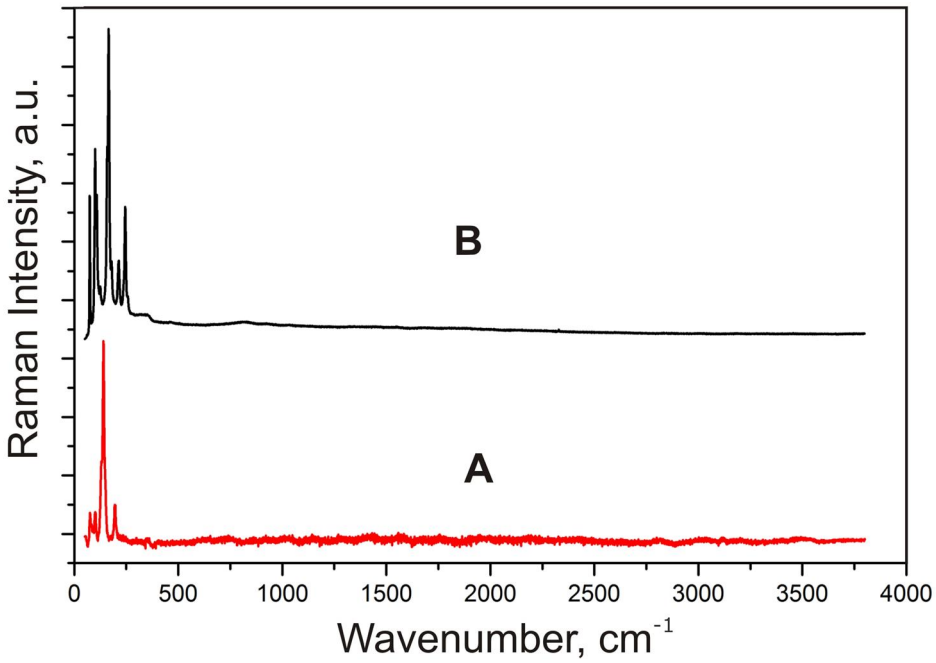

Fig. 2 SM. Typical Raman spectra of chloride mineral inclusions in halite showing the absence of water: $KCaCl_3$ from the chloride segregation in kimberlite of the Udachnaya-East pipe (A); $CaCl_2$ inclusion from the Kochumdek borehole (B).

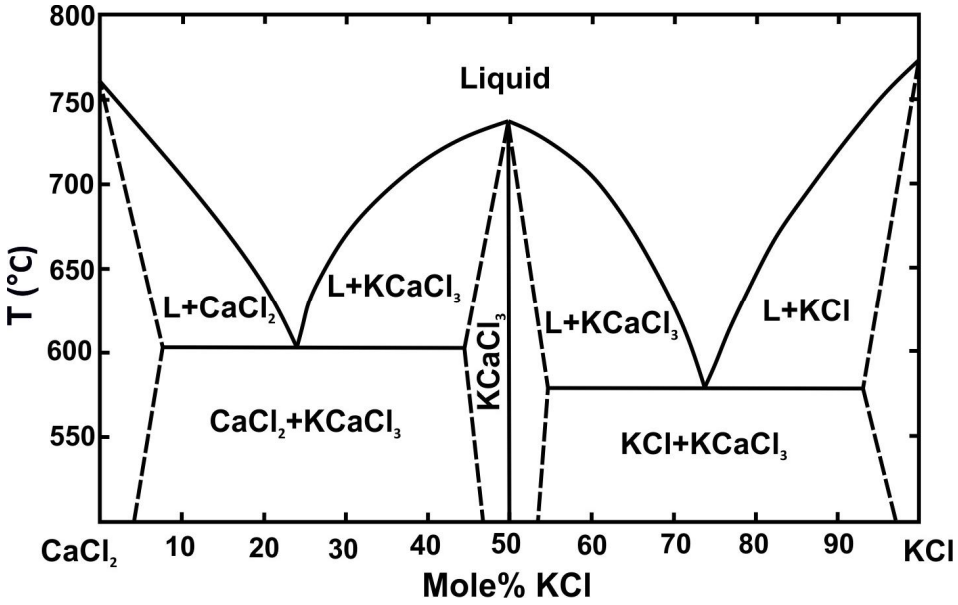

Fig. 3 SM. The phase diagram of the simply binary system KCl−$CaCl_2$ (Robert et.al.,1975)

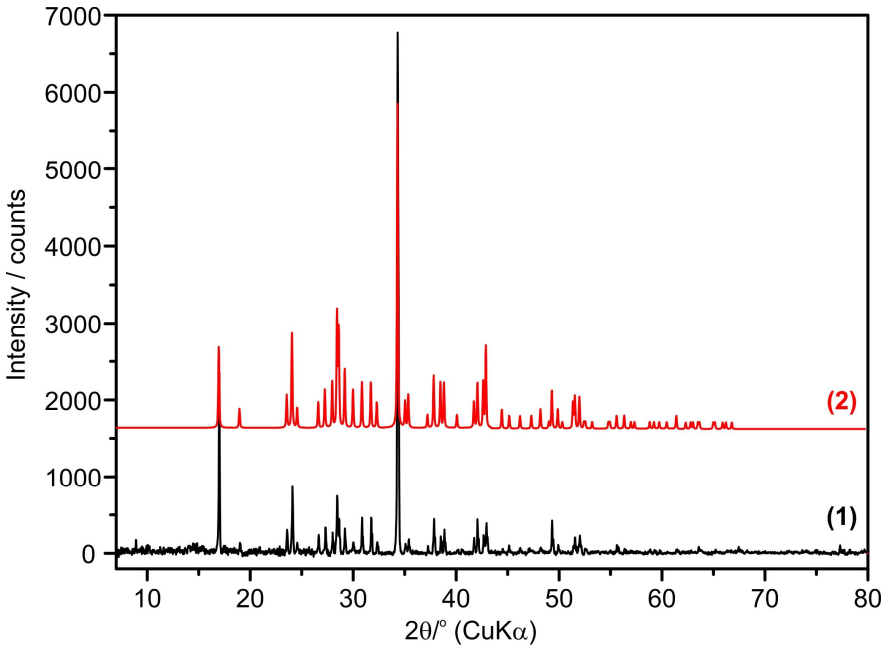

Fig. 4 SM. Comparison of XRD analysis of the synthetic $KCaCl_3$, prepared from the mixture of 1KCl:1$CaCl_2$ (1), with the XRD pattern of $KCaCl_3$ (2) published by Swanson et al (1969). The XRD pattern of $KCaCl_3$ prepared in this study contains all known reflections of $KCaCl_3$ listed by Swanson et al. (1969). No other reflections are observed.

Table 1SM: The positions and intensity of reflections of prepared $KCaCl_3$ sample (this work) and published pattern of $KCaCl_3$ (1969); CuKα_1, λ = 1.54056, temp. = 25°C.

d-spacing				Intensity			
$KCaCl_3^1$		$KCaCl_3^2$		$KCaCl_3^1$		$KCaCl_3^2$	
5.24	1.86	5.23	1.86	31	2	25	2
4.69	1.85	4.68	1.85	2	5	6	12
3.79	1.83	3.78	1.83	4	1	9	6
3.71	1.81	3.70	1.81	12	1	30	2
3.63	1.78	3.62	1.78	2	2	5	8
3.36	1.77	3.35	1.77	3	2	7	10
3.28	1.76	3.27	1.76	5	3	12	10
3.20	1.74	3.19	1.75	3	1	14	2
3.15	1.74	3.14	1.74	10	1	35	2
3.12	1.72	3.12	1.72	5	1	30	2
3.07	1.67	3.06	1.67	4	1	18	2
2.98	1.67	2.98	1.67	2	1	12	2
2.90	1.66	2.90	1.65	6	1	14	4
2.82	1.65	2.82	1.64	6	1	14	4
2.77	1.63	2.77	1.62	2	1	8	2
2.62	1.60	2.61	1.60	100	1	100	2
2.56	1.57	2.56	1.57	2	1	8	2
2.54	1.56	2.54	1.56	2	1	10	2
2.42	1.55	2.41	1.55	1	1	4	2
2.38	1.53	2.38	1.53	6	1	16	2
2.34	1.51	2.34	1.51	3	1	14	4
2.32	1.51	2.32	1.50	4	1	14	2
2.25	1.48	2.25	1.48	1	1	4	2
2.17	1.47	2.16	1.47	2	1	8	2

2.15	1.46	2.15	1.46	5	1	14	2
2.12	1.46	2.12	1.46	3	1	14	2
2.11	1.44	2.11	1.44	5	1	25	2
2.04	1.43	2.04	1.43	0	1	6	2
2.01	1.41	2.01	1.41	1	1	4	2
1.97	1.40	1.96	1.40	1	1	4	2
1.93	1.39	1.92	1.39	1	1		2
1.89	1.86	1.89	1.86	1	2	6	2

Table 2SM. Frequencies of Raman active phonon modes of synthetic and natural $KCaCl_3$ in comparison with calculated obtained using GGA PBESol.

Synthetic	Natural	*Pnma, DFT*	
v, cm^{-1}	*v*, cm^{-1}	*Irreps*.	ν, cm^{-1}
		A_g	52.9
57	57	B_{1g}	55.0
		B_{2g}	61.1
66		B_{3g}	66.6
75	75	A_g	70.4
		B_{2g}	80.1
		B_{1g}	81.4
86	87	A_g	88.9
		B_{3g}	93.8
97	98	A_g	101.5
		B_{2g}	101.7
		B_{2g}	114.5
128	129	B_{1g}	126.7
		B_{3g}	134.3
		A_g	135.0
		B_{2g}	136.6
139	140	A_g	137.5
147	149	B_{2g}	148.7
		B_{1g}	190.6
192	194	A_g	191.7
		B_{3g}	192.6
		B_{1g}	233.0
		B_{2g}	237.4
		B_{3g}	245.29